ARTICLE IN PRESS

Catalysis Today xxx (xxxx) xxx-xxx



Contents lists available at ScienceDirect

Catalysis Today

journal homepage: www.elsevier.com/locate/cattod



Characterization and catalytic behavior of Fischer–Tropsch catalysts derived from different cobalt precursors

Xu Li^a, Haider Almkhelfe^a, Nicholas M. Bedford^b, Tyson C. Back^c, Keith L. Hohn^a, Placidus B. Amama^{a,*}

- ^a Tim Taylor Department of Chemical Engineering, Kansas State University, Manhattan, KS 66506, USA
- b School of Chemical Engineering, University of New South Wales, Sydney, NSW, 2052, Australia
- ^c Materials and Manufacturing Directorate, Air Force Research Laboratory, WPAFB, OH 45433, USA

ARTICLE INFO

Keywords: Fischer–Tropsch Co catalysts Co precursors C5+ selectivity

CO conversion

ABSTRACT

1. Introduction

Concerns about dwindling crude-oil reserves and their negative impact on the environment are forcing researchers to seek new routes that yield clean fuels and chemicals [1,2]. Fischer–Tropsch synthesis (FTS) provides a pathway for the transformation of biomass, coal or natural gas into fuels and chemicals using a transition metal, such as Fe, Co, or Ru, as a catalyst [3,4]. Among these catalysts, Ru-based types exhibit the highest activity and C5+ selectivity [5]. However, due to the high cost of Ru, its widespread use in FTS is limited [6]. Although Fe is an earth-abundant transition metal, it is plagued by its high watergas shift (WGS) reaction activity, thus lowering C5+ selectivity [7,8]. Conversely, Co-based catalysts exhibit relatively higher activity and selectivity to long-chain paraffins, high resistance to deactivation, and a low WGS reaction activity [9,10]. Therefore, well-dispersed Co-based catalysts supported on silica or alumina are generally preferred in FTS.

A number of studies have demonstrated high dependence of catalytic performance on the type of catalyst precursor [11–13] and synthesis method used [14–16]. Iglesia's group has shown the turnover

frequency (TOF) of Co catalysts is dependent on the concentration of active sites and independent of the nature of support and dispersion of Co catalysts [17-19]. While different precursors have been used to synthesize Co-based FT catalysts, the most commonly used precursor is Co(NO₃)₂ [3]. Unlike Co catalysts derived from Co(NO₃)₂, those derived from Co(C2H3O2)2, as reported by Girardon et al. [20], exhibit low reducibility; the study also reveals that catalysts derived from Co (C2H3O2)2 easily form a hard-to-reduce compound during calcination thereby limiting FTS activity. On the contrary, work by Zhang and coworkers [21] revealed that γ-Al₂O₃-supported catalysts prepared from Co(C₂H₃O₂)₂ tend to form CoO after thermal treatment in N₂, which shows higher activity than Co₃O₄ prepared from Co(NO₃)₂. SiO₂supported Co catalysts derived from CoCl2, as reported by Bae et al. [12], show low FTS activity and C5+ selectivity because the residual chloride ions (Cl⁻) poison the catalyst during FTS reaction. Panpranot et al. [22] attribute the low FTS performance of Co catalysts prepared from CoCl₂ to the blockage of catalytic sites by residual Cl⁻. A series of Co carbonyl clusters were also used as Co precursors in preparation of FTS catalysts [23]; the dispersion of Co catalysts prepared from Co

https://doi.org/10.1016/j.cattod.2019.05.023

Received 1 October 2018; Received in revised form 24 April 2019; Accepted 11 May 2019 0920-5861/ © 2019 Elsevier B.V. All rights reserved.

^{*} Corresponding author.

Table 1
Summary of properties of catalyst support and fresh cobalt catalysts derived from different cobalt precursors.

Catalysts	Name	Surface Area (m²/g)	Total Pore Volume (cm ³ /g)	Average Pore Size (Å)	BET C Constant	$d_{(Co3O4)}{}^a(nm)$	$d_{(Co3O4)}{}^b(nm)$	Reducibility (%)
Co(NO ₃) ₂ /SiO ₂	Co-Nit	316.8	0.64	81.5	107.7	3.7	11.4	94.77
$Co(C_2H_4O_2)_2/SiO_2$	Co-Ace	336.0	0.70	83.9	101.1	3.0	25.9	88.82
CoCl ₂ /SiO ₂	Co-Chl	331.3	0.72	87.1	97.4	2.8	35.4	64.24
Co(OH) ₂ /SiO ₂	Co-Hyd	432.3	0.97	89.9	132.2	4.0	25.7	91.06
SiO_2	-	457.0	1.02	90.0	123.7	-	-	-

^a Average catalyst diameter from TEM.

^b Average crystallite size from XRD.

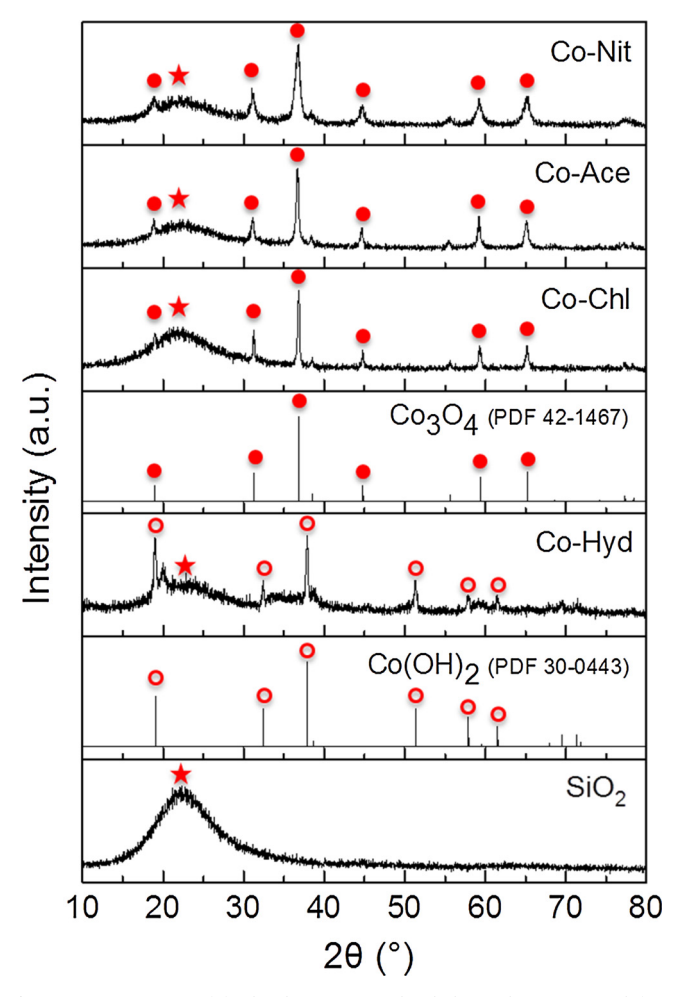


Fig. 1. XRD patterns of fresh silica-supported cobalt catalysts prepared from different cobalt precursors $[Co(NO_3)_2, Co(C_2H_3O_2)_2, CoCl_2, and Co(OH)_2]$.

carbonyl clusters exhibits better catalytic activity than those prepared from $Co(NO_3)_2$. Unlike FT catalysts derived from traditional precursors, cobalt carbonyl clusters are able to provide metallic particles in their zero valent state and, therefore, do not require aggressive reduction treatment. However, synthesis of Co carbonyl clusters results in catalysts with different surface acidities that affect CO conversion and C5+ selectivity [23].

In our previous investigation, we showed that cobalt hydroxide is a promising precursor for synthesis of well-dispersed Co catalysts on carbon nanotubes (CNTs) via a modified photo-Fenton process [15]. The resulting CNT-supported Co catalyst does not require a calcination step and is free of possible catalyst inhibitors usually present in conventional catalyst precursors such as nitrates, chlorides, acetates, and carbonyls; FTS reaction with this catalyst shows high CO conversion (*80%) and outstanding C5+ selectivity (*70%). In all, a number of Co precursors have been used for synthesis of Co catalysts on SiO₂ support

[12,20,24–26]; however, some fundamental questions related to how precursor type affects catalyst reducibility, hydrocarbon product distribution, and catalyst lifetime remain unanswered. The behavior of catalysts derived from a green precursor (Co(OH)₂) and supported on a conventional substrate such as SiO₂ or Al₂O₃ is, however, noteworthy.

eMotivated by the lack of understanding of the effect of precursor type (including a novel 'green' precursor) on FTS catalysis, this study investigates the properties and catalytic performance of SiO₂-supported Co catalysts derived from Co(OH)2, Co(NO3)2, Co(C2H3O2)2, and CoCl2 via incipient wetness impregnation. The synthesized catalysts are characterized using a wide range of techniques including transmission electron microscopy and spectroscopy (TEM), X-ray diffraction (XRD), temperature-programmed reduction (TPR), X-ray photoelectron spectroscopy (XPS), and X-ray absorption spectroscopy (XAS). In addition, the catalytic performance (CO conversion, C5+ selectivity, and C5+ product distribution) and stability of the synthesized catalysts during FTS are evaluated and compared. Further, post-mortem characterization of the catalysts are conducted using TEM, XAS, and XRD to elucidate structural and chemical changes. The results illuminate how the type of cobalt precursor (including cobalt hydroxide) affect catalyst structure, reducibility, and FTS performance (turnover frequency, stability and hydrocarbon product distribution).

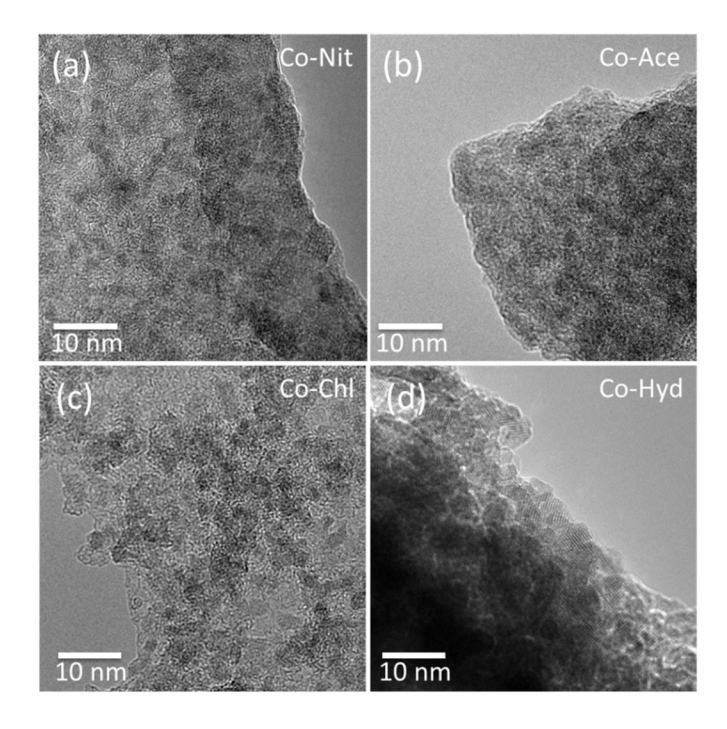
2. Experimental

2.1. Catalyst preparation

Co/SiO2 catalysts were synthesized via conventional incipient wetness impregnation from different Co precursors: Co(NO₃)₂·6H₂O (Aldrich, $\geq 98\%$ purity), Co(C₂H₃O₂)₂·4H₂O (Aldrich, $\geq 98\%$ purity), CoCl₂·6H₂O (Aldrich, ≥98% purity), and Co(OH)₂ (Strem, ≥97% purity). Catalyst solutions were prepared by dissolving each precursor in water except for Co(OH)2, which was dissolved in hydrogen peroxide (30%), a good solvent for Co(OH)₂ that is free of possible catalyst inhibitors. Based on prior studies [27,28], the possibility of Co(OH)₂ and H₂O₂ reacting to form CoO(OH), under our synthesis conditions, is unlikely because the mixture was maintained at room temperature in the absence of NaOH. Silica gel (Aldrich, pore size 60 Å, 100 mesh) was used as a catalyst support. Impregnation of the prepared catalyst solutions in SiO₂ resulted in a catalyst loading of ca. 20 wt%. Thereafter, all freshly synthesized SiO₂-supported Co catalysts were dried at 120 °C, followed by calcination at 550 °C for all catalysts except those synthesized from Co(OH)2. SiO2-supported Co catalysts prepared using Co (NO₃)₂, Co(C₂H₃O₂)₂, CoCl₂, and Co(OH)₂ are designated as Co-Nit, Co-Ace, Co-Chl, and Co-Hyd, respectively. Calcined Co-Nit, Co-Ace, and Co-Chl catalysts, as well as uncalcined Co-Hyd, were used for catalytic testing, and are hereafter referred to as fresh catalysts.

2.2. Catalyst characterization

Textural properties of the catalysts were determined by N_2 physisorption at $-196\,^{\circ}\text{C}$ using an Autosorb-1 series system. Prior to physisorption measurements, all the fresh catalysts were outgassed at 250 $^{\circ}\text{C}$ for 10 h. The Brunauer-Emmet-Teller (BET) method [29] was



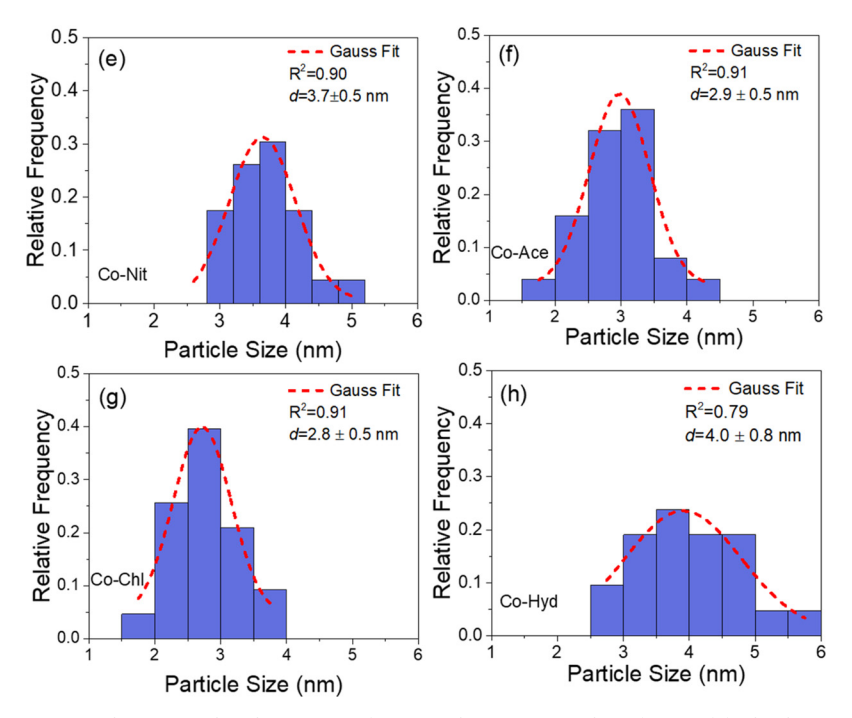


Fig. 2. High-magnification TEM images and corresponding histograms of PSDs with Gaussian analysis fitting of fresh silica-supported catalysts prepared from different cobalt precursors: $Co(NO_3)_2$ (a and e), $Co(C_2H_3O_2)_2$ (b and f), $CoCl_2$ (c and g), and $Co(OH)_2$ (d and h).

applied to the adsorption isotherm in the linear range of relative pressure from 0.02 to 0.35 to determine the specific surface area of each catalyst. Pore size distribution was determined from the desorption branch at a relative pressure of 0.95 of the isotherm using the Barrett-Joyner-Halenda (BJH) model [30].

XRD analyses were conducted to identify atomic and molecular structures of fresh catalysts. XRD patterns were recorded on a Rigaku Miniflex II desktop X-ray diffractometer using Cu K α radiation ($\lambda=1.54056\,\mbox{Å}$) in the range of $10^\circ<2\theta<80^\circ$ with a step size of 0.10° and scan speed of $1.00^\circ/min$. The average crystallite size of Co_3O_4 in

the fresh catalysts was estimated by the Scherrer equation (Eq. 1) [31], where $d_{Co_3O_4}$ is average crystallite size, $\lambda=1.54056$ Å, β is full width at half maximum (FWHM), and $2\theta=36.9^\circ$.

$$d_{Co_3O_4} = \frac{0.94\lambda}{\beta cos\theta} \tag{1}$$

The actual Co loading ratio of fresh catalysts was verified by inductively coupled plasma atomic emission spectroscopy (ICP-Varian 720-ES).

The reducibility of fresh catalysts was studied by temperature

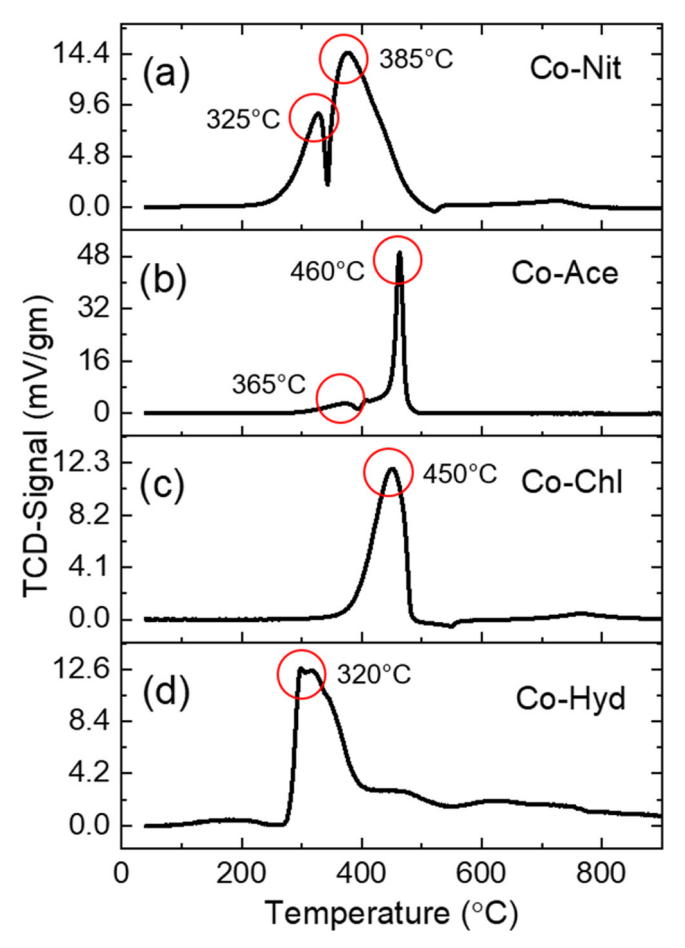


Fig. 3. H₂-TPR profiles of silica-supported cobalt catalysts prepared from different precursors: (a) (Co(NO₃)₂, (b) Co(C₂H₃O₂)₂, (c) CoCl₂, and (d) Co(OH)₂.

programmed reduction (TPR) in an AMI-200 catalyst characterization system equipped with a thermal conductivity detector. 0.1 g of sample was put into a U-shaped quartz tube and pre-treated to remove moisture and impurities under helium flow (30 ml/min) at 140 °C for 1 h. Thereafter, the sample was cooled to 40 °C and heated again to 900 °C at a ramping rate of 10 °C/min under a flow of 10% $\rm H_2$ in Ar at 30 ml/min while the hydrogen consumption was measured. The reducibility of the catalyst ($R_{\rm CO}$) was calculated using Eq. 2:

$$R_{Co} = \frac{reduced\ amount\ of\ Co}{total\ amount\ of\ Co} \times 100\% \tag{2}$$

The steps for calculating the reduced amount of Co from the TPR profile are presented in the Supplementary Information.

To characterize the catalyst morphology, TEM images were obtained using (FEI Tecnai F20 XT) operating at 200 kV. The samples were dropped on a copper microgrid coated with lacey carbon film.

XPS measurements were performed on a Kratos Ultra XPS system with a base pressure of $1.0\times10^{-9}\,\text{Torr}$. Spectra were acquired with a monochromatic Al K α source (h $\nu=1486.6\,\text{eV}$). The X-ray source was operated at 10 mA and 12 keV (120 W). A charge neutralizer was used to reduce the effect of charging. Survey (high-resolution) spectra were acquired at 160 (20) eV pass energy with 1.0 (0.1) eV steps with 100 ms dwell times. Analysis of XPS spectra was performed using CasaXPS software. All elemental regions were fit with a Shirley background. Components in the high-resolution spectra were fit with a combination of Gaussian and Lorentzian peak shapes. These peaks are represented by the LA lineshape in CasaXPS. The fitting routine used a Levenburg–Marquardt routine to minimize χ^2 . Relative sensitivity factors were based on Scofield cross sections. Peak positions were initially

constrained based on previously reported values by Biesinger et al. [32].

X-ray absorption near-edge structure (XANES) and edge X-ray absorption fine structure (EXAFS) were performed at the Inner Shell Spectroscopy beamline at the National Synchrotron Light Source-II. Samples were diluted with BN and pressed into pellets for measurements in a transmission geometry. Data were collected from ~200 eV below the Co K-edge (7709 eV) to ~1100 past the Co K-edge. Data processing and subsequent structure modeling were performed with the Athena and Artemis data packages, respectively [33], wherein a ${\rm S_0}^2$ value of 0.812 was used in calculations and obtained from modeling the EXAFS from a reference Co foil. Known bulk structures for metallic Co, ${\rm Co_3O_4}$, ${\rm CoO}$, and ${\rm \beta\text{-}Co(OH)_2}$ where used in EXAFS modeling when needed while a computed CoOOH structure from the materials project was used for certain scattering paths [34].

2.3. Catalytic testing

The activity and product selectivity of catalysts were evaluated using a stainless steel tubular fixed-bed reactor 1/2-inch in diameter. Typically, 2 g of catalyst mixed with 8 g of SiC was loaded into the reactor. SiC is an inert diluent material with high thermal conductivity (k = 4 W/cm K) used to enhance temperature uniformity across the reaction bed [35]. Prior to FTS reaction, each catalyst was activated at the optimum reduction temperature determined from TPR data. Co-Nit and Co-Hyd catalysts were reduced in situ by flowing 100 sccm H2 and 100 sccm N2 under atmospheric pressure for 12 h at 350 °C while Co-Ace and C-Chl were reduced in situ at 450 °C under similar conditions. After reduction, the reactor was cooled to 120 °C under flowing N₂, followed by increasing the pressure to 150 psi by introducing 100 sccm H₂, 50 sccm CO, and 100 sccm N₂. Next, the temperature was slowly increased to 230 °C at a heating rate of 1 °C/min to prevent instability associated with the highly exothermic FTS reaction. The reaction was allowed to run for 30 h. Once steady state was achieved, the reaction was allowed to proceed for 15 h. The stream of effluents from the reactor was depressurized to atmospheric pressure through a pressurerelief valve and passed through a heated line maintained at 150 °C with a heating tape attached to an online gas chromatograph (GC, SRI-8610C) equipped with a TCD, FID, and methanizer.

CO conversion was calculated according to Eq. 3, where $F_{CO,in}$ is inlet CO molar flow rate and $F_{CO,out}$ is outlet CO molar flow rate.

$$CO conversion (\%) = \frac{F_{CO,in} - F_{CO,out}}{F_{CO,in}}$$
(3)

Product selectivity was calculated based on Eq. 4, where n is the carbon number of product (C_n) ; $F_{Cn, out}$ is the outlet molar flow rate of product C_n .

Selectivity (%) =
$$\frac{nF_{Cn, out}}{F_{CO, in} - F_{CO, out}}$$
 (4)

The chain-growth probability (α) was obtained from the Anderson–Schultz–Flory chain-length statistics equation (Eq. 5) [36], where W_n is the mass fraction of the species with carbon number n. From the slope of the plot of $\ln (W_n/n)$ against n, the value of α can be obtained.

$$\ln\left(\frac{W_n}{n}\right) = nln\alpha + const\tag{5}$$

TOF based on catalyst reducibility data from TPR was determined from:

$$TOF = \frac{-r_{CO}M_{Co}}{D_{Co}x_{Co}} \tag{6}$$

where $-r_{CO}$ is the CO reaction rate, M_{Co} is atomic weight of Co, x_{Co} is the weight ratio of Co in the catalyst, and D_{Co} is the Co dispersion.

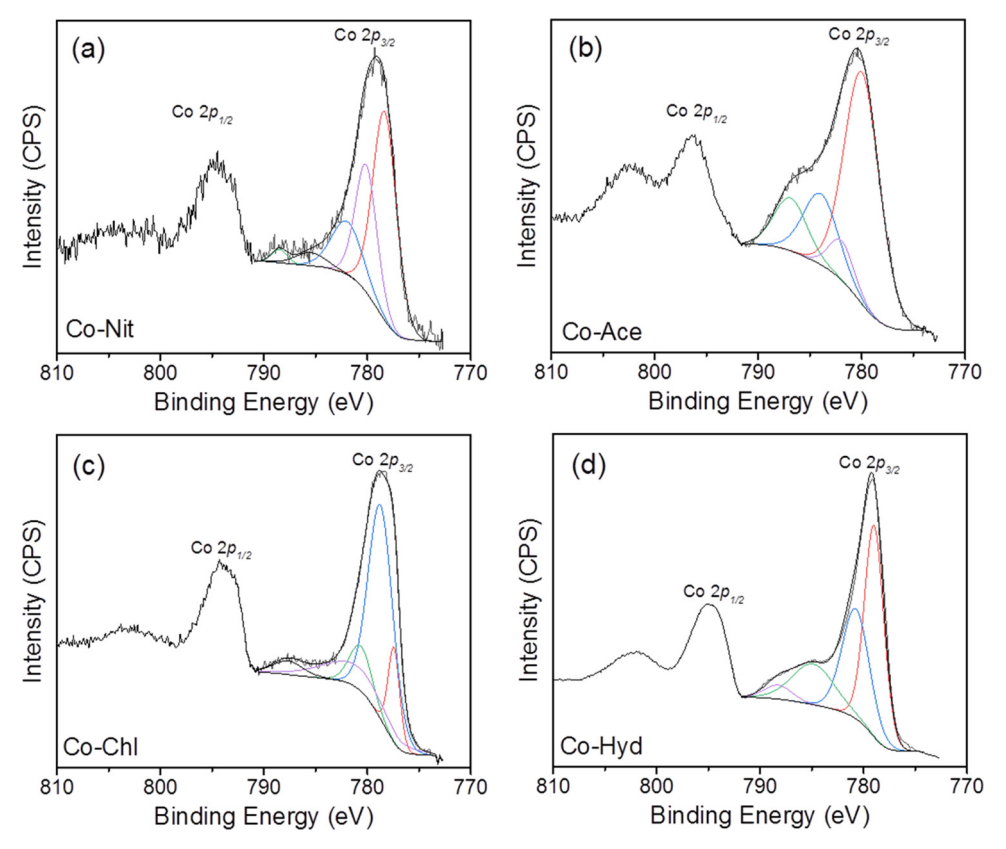


Fig. 4. XPS spectra of silica-supported cobalt catalysts prepared from different precursors: (a) Co(NO₃)₂, (b) Co(C₂H₃O₂)₂, (c) CoCl₂, and (d) Co(OH)₂.

 Table 2

 Catalytic activity and product selectivity of fresh silica-supported cobalt catalysts derived from different precursors obtained at steady state after 15 h on stream.

Catalysts	Name	CO Conversion (%)	Hydrocarbon Selectivity (%)			FTS Reaction Rate (g HC/h*g-cat.)	TOF (10 ⁻⁴ s ⁻¹)	α
			CH ₄	C2-C4	C5+			
Co(NO ₃) ₂ /SiO ₂	Co-Nit	56	27	17	56	0.53	10.4	0.75
$Co(C_2H_4O_2)_2/SiO_2$	Co-Ace	12	46	2	52	0.11	1.9	0.91
CoCl ₂ /SiO ₂	Co-Chl	7	52	1	47	0.06	1.5	0.88
Co(OH) ₂ /SiO ₂	Co-Hyd	60	38	3	59	0.56	12.7	0.86

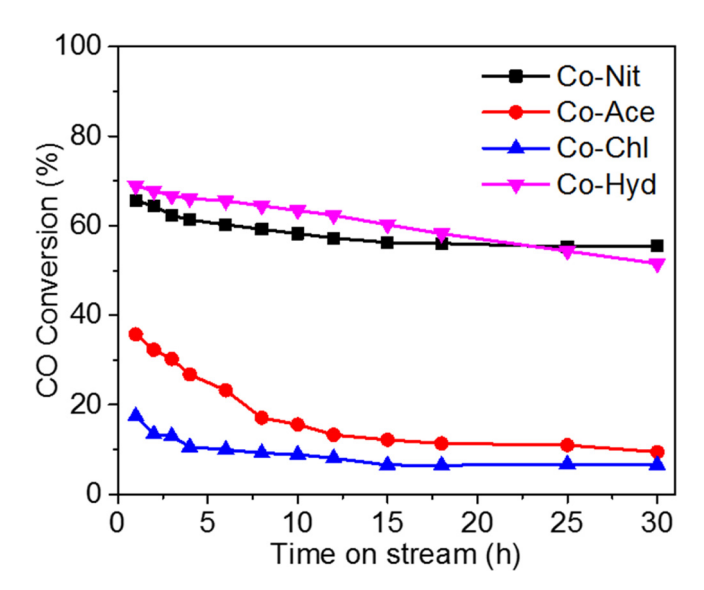


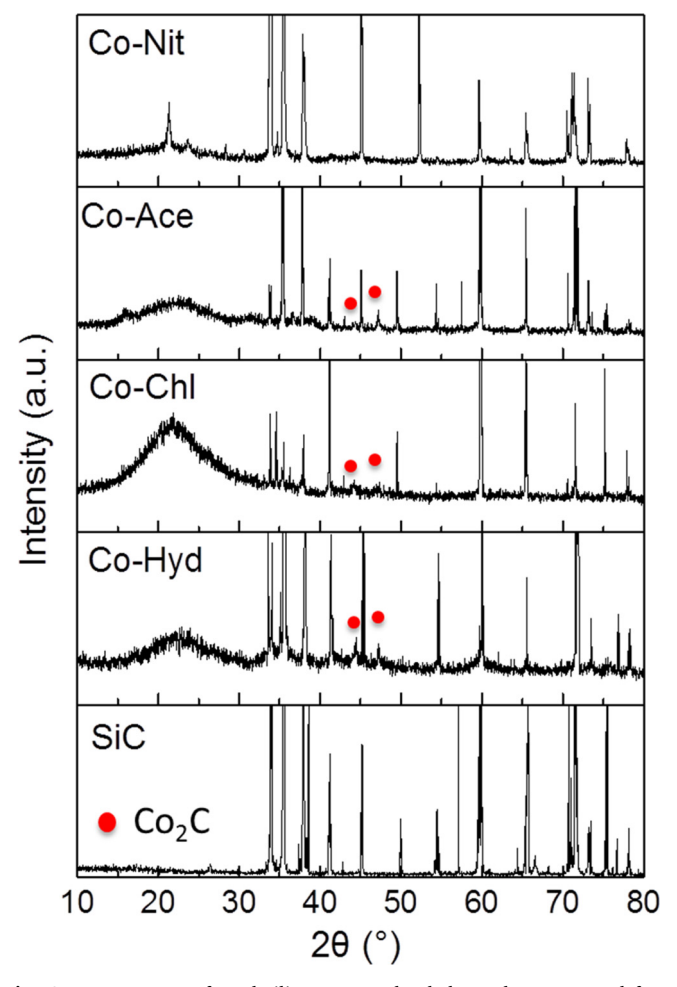
Fig. 5. CO conversion as a function of time on stream using silica-supported cobalt catalysts prepared from different precursors $[(Co(NO_3)_2, Co(C_2H_3O_2)_2, CoCl_2, and Co(OH)_2].$

3. Results and discussion

3.1. Catalyst characterization

3.1.1. Nitrogen adsorption-desorption

A summary of the properties of fresh catalysts is presented in Table 1. The BET specific surface area (SA_{BET}) of Co-Nit, Co-Ace, and Co-Chl are 317, 336, and 331 m²/g, respectively. In contrast, Co-Hyd exhibits a relatively higher SA_{BET} of 432 m²/g, which is close to that of pristine SiO₂ support. This result suggests the absence of calcination in preparation of Co-Hyd allows SiO2 (support material) to preserve its structural properties. Total pore volume and pore diameter of the catalysts increase in the following order: Co-Nit < Co-Ace < Co-Chl < Co-Hyd. The results also show the surface area, total pore volume, and pore diameter decrease after Co impregnation, which is in agreement with previous studies [37,38]. An increase in catalyst pore diameter has been shown to improve FTS activity [8,39]. It is noteworthy that catalysts derived from different precursors exhibit different pore structures with Co-Hyd showing the highest pore diameter. Although the standard incipient wetness impregnation method usually yields catalysts with decreased surface area and pore diameter [40], the opposite effect is observed in the case of Co-Hyd, possibly due to the absence of a calcination step that prevents catalyst sintering and unfavorable



 $\label{eq:Fig. 6. XRD patterns of used silica-supported cobalt catalysts prepared from different precursors [(Co(NO_3)_2, Co(C_2H_3O_2)_2, CoCl_2, and Co(OH)_2].$

interactions between catalyst support and active phase prior to FTS.

3.1.2. X-ray diffraction

XRD patterns of the freshly prepared catalysts (Co-Nit, Co-Ace, Co-Chl, and Co-Hyd) are shown in Fig. 1. The wide diffraction peak at 20 of 22.3°, ascribed to SiO₂ support, is apparent in all diffraction patterns. Co-Nit, Co-Ace, and Co-Chl show diffraction peaks at 20 of 19.0°, 31.3°, 36.9°, 44.8°, 59.4°, and 65.2° due to the presence of crystalline Co₃O₄ spinel (PDF 42–1467) [8]. For Co-Hyd, diffraction peaks at 20 of 19.0°, 32.5°, 37.9°, 51.4°, 57.9°, and 61.5° are indicative of the presence of β -Co(OH) $_2$ (PDF 30-0443) [28]. It can be concluded from the XRD data that Co exists in the form of Co $_3$ O $_4$ in all fresh catalysts except Co-Hyd, where the composition is mainly Co(OH) $_2$. As shown in Table 1, the estimated crystallite size obtained from XRD using the Scherrer equation are in the range of 11–35 nm.

3.1.3. Transmission electron microscopy

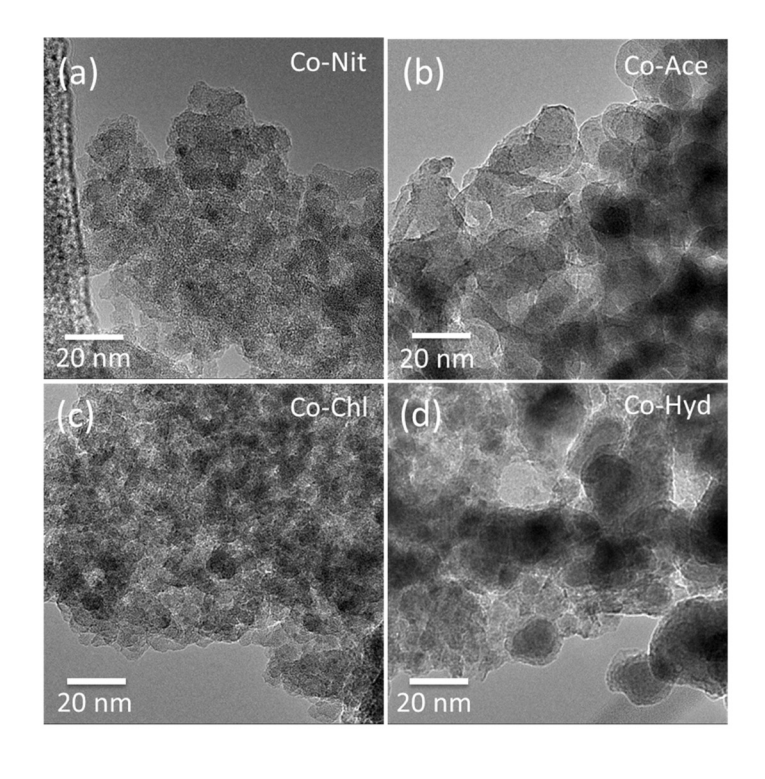
Fig. 2 shows high-magnification TEM images of freshly prepared Co-Nit, Co-Ace, Co-Chl, and Co-Hyd, and their corresponding histograms of particle size distributions (PSDs) with Gaussian analysis fittings. The high-magnification images reveal small catalyst particles that are well-dispersed on SiO_2 support for all fresh catalysts. As the histograms show, all fresh catalysts have particle sizes and standard deviations that are rather similar. However, low-magnification images (Fig. S1) of all fresh catalyst reveal the presence of a small fraction of large particles in the range of 20–30 nm that are not apparent in the high-magnification images. The discrepancy in average particle size obtained from XRD and high-magnification TEM may be due to the limited sensitivity of

XRD to the presence of very small crystallite particles of cobalt oxides; in particular, particles ~3 nm, the approximate average size of particles from high-magnification TEM, are poorly detected by XRD [41]. As the analysis of TEM and XRD data (Table S1) shows, the number density of small particles are significantly higher than that of large particles by at least a factor of 15 in all catalysts. Interestingly, a comparison of the average particle size acquired from low-magnification TEM and XRD, reveal a trend that is fairly consistent and catalyst sizes that are quite comparable. This confirms that both low-magnification TEM and XRD are in fact measuring particles in the same size range. The overall average particle size of catalysts from low- and high-magnification TEM images is in the range of 4–5 nm, which is quite similar to the range obtained from the high-magnification images in Fig. 2 (3–4 nm).

In spite of the controversy surrounding the so-called particle-size effect in FTS, it is generally accepted that catalyst size has a profound impact on activity and selectivity [9,42–44]. Larger Co particles exhibit higher selectivity for higher molecular weight hydrocarbons due to the formation of $-\mbox{CH}_{2^-}$ intermediate via dissociative adsorption of CO. As verified by TEM, the average catalyst size for Co-Nit, Co-Ace, Co-Chl, and Co-Hyd are in the narrow range of 3–4 nm, which minimizes the influence of particle size during FTS and allows for meaningful comparison and the isolation of the intrinsic role of precursor type and catalyst properties.

3.1.4. Hydrogen temperature-programmed reduction (H_2 -TPR)

H₂-TPR profiles presented in Fig. 3 show the reduction behavior of the SiO₂-supported cobalt catalysts. Typically, a Co₃O₄ undergoes a two-step reduction process. The first step, which occurs at a relatively lower temperature, involves reduction of Co₃O₄ to CoO while the second step that occurs at a relatively higher temperature involves reduction of CoO to Co⁰ [8,45]. In Fig. 3a, it is clear the reduction of Co-Nit occurs in two steps, the first at 325 °C and the second at 385 °C. Fig. 3b shows a single peak at 460 °C and a small bump at 365 °C, which may indicate the presence of mixed oxides (CoO and Co₃O₄) for Co-Ace. The small bump at 365 °C is attributed to the reduction of Co₃O₄ to CoO. Thus, TPR results suggest CoO is the main cobalt phase in Co-Ace catalyst. In support of our TPR peak assignment, a number of studies [20,46,47] have shown the presence of only a small fraction of Co species in the form of Co₃O₄ in Co catalyst prepared from cobalt acetate. In our case, we speculate that the dominant CoO particles in Co-Ace are too small to be detected by XRD; the observed XRD pattern for Co-Ace is mostly from a small fraction of large Co₃O₄ particles observed in the low-magnification TEM images (Fig. S1). The absence of a high-temperature reduction peak (> 600 °C) for Co-Ace indicates relatively weak catalyst-support interactions. Conversely, the small and illdefined high-temperature reduction peaks in the profiles of Co-Hyd, Co-Nit, and Co-Chl are evidence of strong catalyst-support interaction and possible formation of irreducible compounds. Because calcination, reduction, and FTS reaction were conducted at temperatures below 600 °C, the observed catalyst-support interactions is not expected to contribute to catalyst deactivation. Fig. 3c shows only one broad peak at 450 °C for Co-Chl that is most likely due to the overlap of the two reduction peaks associated with Co₃O₄. The TPR profile of Co-Hyd is shown in Fig. 3d and the peak at 320 °C is the only intense peak with a distinct shoulder at a higher reduction temperature. As confirmed by XRD (Fig. 1), Co-Hyd contains mainly Co(OH)2. Yang et al. [28] showed that Co(OH)2 decomposes at 130 °C to form Co3O4 via a dehydrogenation reaction; this indicates that there is the possibility of simultaneous decomposition and reduction during TPR. XRD analysis of samples annealed in either N2 or H2 at 300 and 400 °C revealed interesting results (Fig. S2): (1) Co₃O₄ is the main product after annealing Co (OH)2 in N2 at 300 °C, but a small fraction of CoO begins to form at 400 °C; (2) annealing in H₂ at 300 °C yields mixed Co species (Co₃O₄, CoO and Co metal) while at 400 °C, metallic Co is obtained. Therefore, TPR of Co(OH)₂ forms Co₃O₄ and CoO that are subsequently reduced to Co metal as reduction progresses. The results also suggest that Co(OH)2



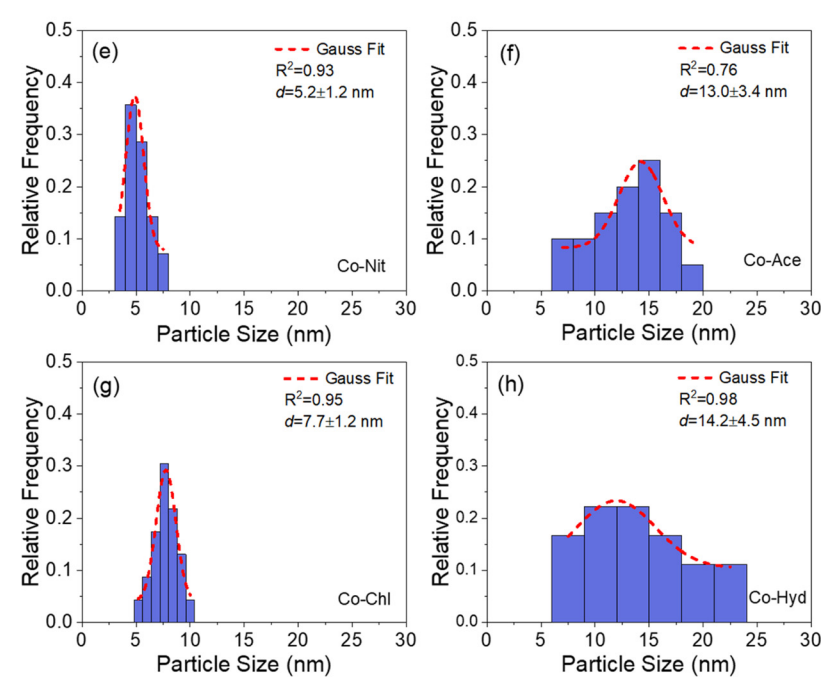


Fig. 7. High-magnification TEM images and corresponding histograms of PSDs with Gaussian analysis fitting of used silica-supported catalysts prepared from different precursors: $Co(NO_3)_2$ (a and e), $Co(C_2H_3O_2)_2$ (b and f), $Co(C_1C_2H_3O_2)_2$ (b and f), and $Co(OH)_2$ (d and h).

is fully reduced at 400 °C in $\rm H_2$ irrespective of the decomposition products formed during annealing. The possible existence of $\rm Co^{3+}$ and $\rm Co^{2+}$ in Co-Hyd is consistent with the broad TPR peak observed. Moreover, the broad peaks between 600 °C and 800 °C for Co-Nit, Co-Chl and Co-Hyd correspond to the reduction of Co species with strong interactions with $\rm SiO_2$ support [39,44,48]. Acetate-derived catalysts are known to readily form hard-to-reduce compounds during annealing; the absence of high-temperature peaks in Co-Ace may be due to prior formation of silicates during calcination. We emphasize that among the four catalysts, Co-Hyd exhibits the lowest reduction temperature, and is, therefore, the most easily activated under FTS reaction conditions.

From Fig. 3, reduction temperatures of Co-Nit and Co-Hyd are below 400 °C while those of Co-Ace and Co-Chl are higher. As a result, the two sets of catalysts, those with lower (Co-Nit and Co-Hyd) and higher reduction temperatures (Co-Ace and Co-Chl), were reduced at 350 °C and 450 °C prior to FTS, respectively. The reducibility of catalysts increases in the following order: Co-Chl (64.2%) < Co-Ace (88.8%) < Co-Hyd (91.1%) < Co-Nit (94.8%). Basically, this trend is somewhat consistent with the reduction temperatures of the catalysts as evidenced by Co-Hyd and Co-Nit that reduce at low temperatures showing high reducibility (> 90%). Unlike Co-Hyd and Co-Nit, the relatively low reducibility of Co-Chl (64.24%) indicates the presence of

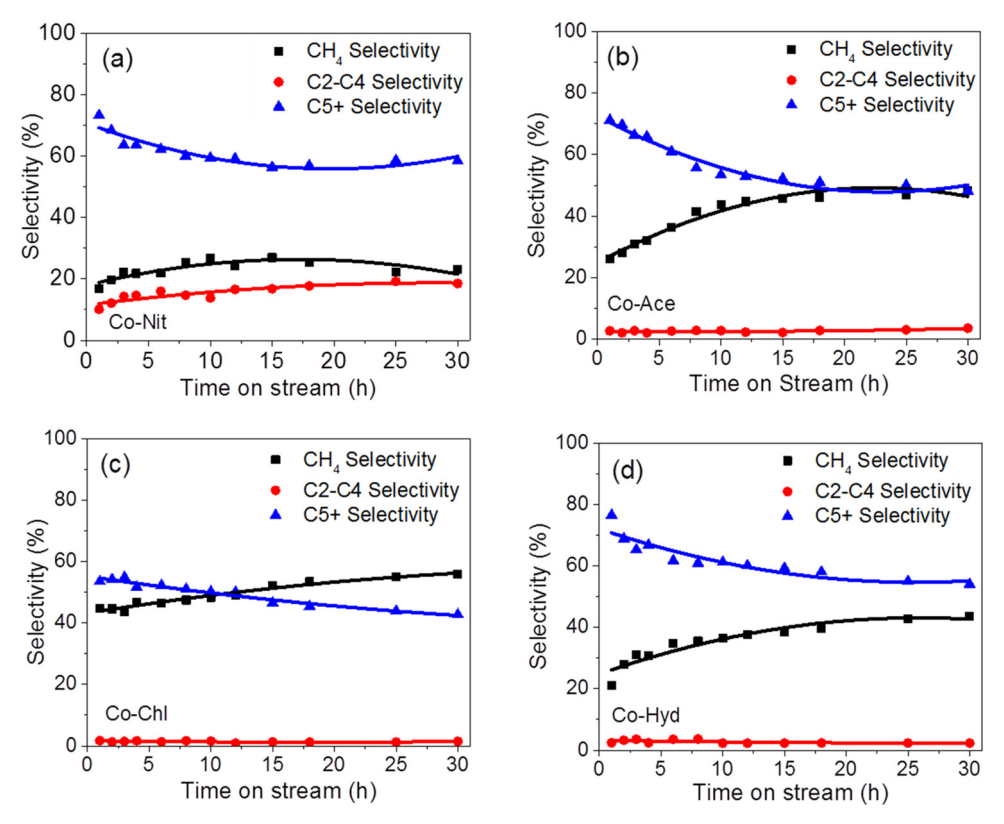


Fig. 8. Hydrocarbon selectivity of silica-supported cobalt catalysts prepared by different Co precursors: (a) Co(NO₃)₂, (b) Co(C₂H₃O₂)₂, (c) CoCl₂, and (d) Co(OH)₂.

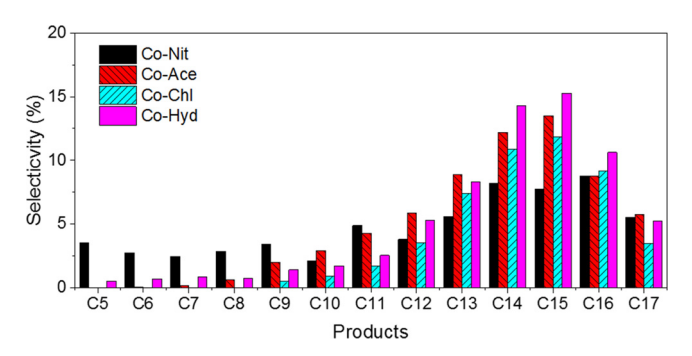


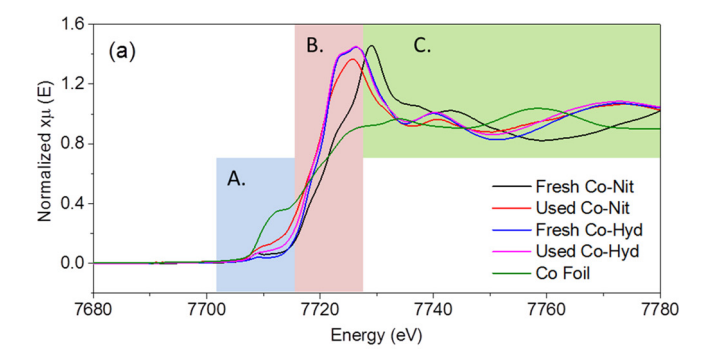
Fig. 9. C5+ products distributions for silica-supported cobalt catalysts prepared from different cobalt precursors [$(Co(NO_3)_2, Co(C_2H_3O_2)_2, CoCl_2, and Co(OH)_2$].

a limited amount of active Co species for catalyzing FTS reaction.

3.1.5. X-ray photoelectron spectroscopy

The high-resolution Co 2p XPS spectra of the fresh catalysts in Fig. 4 show the characteristic doublet (Co $2p_{3/2}$ and $2p_{1/2}$) with satellite peaks from spin-orbit splitting. Because both Co $2p_{3/2}$ and $2p_{1/2}$ peaks qualitatively contain the same information, curve fitting has been restricted to the higher-intensity Co 2p_{3/2} peak. Here an improved curvefitting methodology reported by Biesinger et al. [32] is used for interpretation of 2p spectra of Co (details are not provided here to avoid duplication). The Co $2p_{3/2}$ peak and shake-up satellite features for Co-Nit and Co-Chl are centered on 779.3 and 789.0 eV, respectively. Evidently, distinct shake-up satellite features for Co $2p_{3/2}$ and Co $2p_{1/2}$ are present in the spectra from Co-Nit and Co-Chl, and the satellite peak observed ~789.0 eV is used to confirm the presence of Co₃O₄ [3,49,50]. The so-called 'shake-up' features are associated with either a coupling between unpaired electrons in the atom or a multiple-electron excitation [28]. Also, an intense Co 2p peak accompanied by a satellite peak of low intensity is associated with formation of Co₃O₄ [51]; the presence of these features in the spectra of Co-Nit and Co-Chl is further evidence of Co existing as Co₃O₄, in agreement with XRD results (Fig. 1). Co 2p spectrum of Co-Hyd is similar to the standard spectrum for Co(OH)2 reported by Biesinger et al. [32], with shake-up satellite features of Co 2p3/2 peak components that shift to lower-binding energies at 784.9 eV and 788.3 eV [28,32]. Therefore, Co-Hyd is mainly composed of Co(OH)2, in agreement with XRD results (Fig. 1). The composition of Co-Hyd as revealed by XPS is unsurprising, as it does not undergo calcination that could have induced thermal decomposition to its oxide. In the case of Co-Ace, Co 2p3/2 and corresponding satellite peaks are centered around 780.4 and 786.7 eV [32,51], suggesting a Co²⁺ state that is most likely CoO; interestingly, this is inconsistent with XRD data (Fig. 1) as peaks from Co-Ace are indexed as Co₃O₄. All Co 2p_{3/2} peak components are summarized in the Supplementary Information (Table S2). The discrepancy in the chemical species identified by XPS and XRD for Co-Ace may be due to the limited sensitivity of XRD to small particles. Low- and high-magnification TEM analysis reveals the presence of a small fraction of large particles in the range of 20-35 nm and a large fraction of small particles ~3 nm. The consistency observed in the variation of the average particle size obtained from low-magnification TEM and XRD (Table S1) is evidence of the selective detection of mainly large particles by XRD. We, therefore, conclude that Co-Ace is composed of a small fraction of large Co₃O₄ particles that are easily detected by XRD and XPS, and a large fraction of small CoO particles that are only detected by XPS. For all fresh catalysts, the number density of small particles are significantly higher than large particles (Table S1); the significance of this result is twofold: First, the large fraction of small particles are the dominant active sites. Second, the result explains why XPS spectrum for Co-Ace is consistent with CoO phase, not Co₃O₄. The observed formation of CoO in Co-Ace is supported by the work of Zhang et al. [21] that revealed the susceptibility of Co catalysts derived from cobalt acetate to form CoO.

To further verify our conclusions, the intensity ratio of the Co $2p_{1/2}$ satellite to its main peak for fresh catalysts is compared; studies [49,52,53] have shown this ratio, which is \sim 0.9 for CoO and \sim 0.3 for



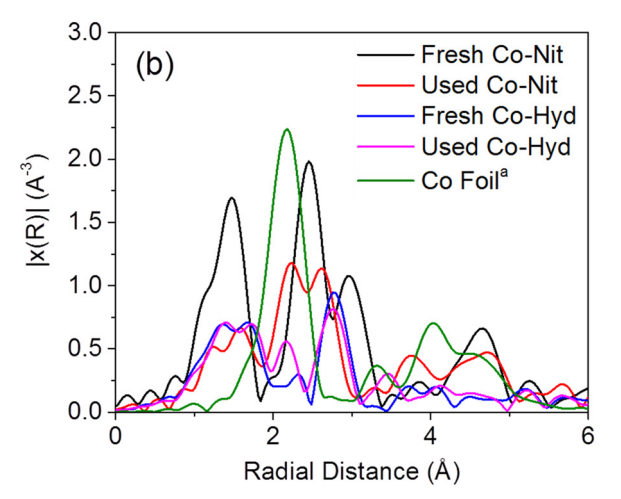


Fig. 10. XANES profiles of freshly prepared and used catalysts prepared from $Co(NO_3)_2$ and $Co(OH)_2$ precursors (a). EXAFS profiles of freshly prepared and used catalysts prepared from $Co(NO_3)_2$ and $Co(OH)_2$ precursors (b). (aintensity of Co foil was reduced by 50%).

 ${\rm Co_3O_4}$, can be used to distinguish between the two oxides. The calculated ratio for Co-Ace, Co-Nit, Co-Chl, and Co-Hyd are 0.5, 0.3, 0.2, and 0.3, respectively. All the samples except for Co-Ace have a ratio that is ${\rm \tilde{c}}$ 0.3, indicating the dominant Co species is present as ${\rm Co_3O_4}$. However, the ratio for Co-Ace is 0.5, between the values expected for CoO and ${\rm Co_3O_4}$, even though the XPS spectrum is consistent with that of CoO. XRD detects only ${\rm Co_3O_4}$ while XPS detects both CoO and ${\rm Co_3O_4}$. We hypothesize the ratio is higher for Co-Ace due to the presence of mixed

oxides, with a low fraction of large ${\rm Co_3O_4}$ particles and a high fraction of small CoO particles. We conclude from XPS data that the Co phase formed is sensitive to the Co precursor used during synthesis. The results reveal the formation of ${\rm Co_3O_4}$ for Co-Nit and Co-Chl while Co-Hyd is composed mainly of ${\rm Co(OH)_2}$, in agreement with XRD data (Fig. 1). On the other hand, Co-Ace yields nanoparticles with a mixed Co phase that is consistent with TPR data.

3.2. FTS activity and selectivity

3.2.1. Activity of SiO₂-supported cobalt catalyst

The catalytic activity and product selectivity of the different catalysts are summarized in Table 2. It is apparent from the results that catalytic activity is strongly affected by the type of Co precursor used during synthesis. CO conversions of Co-Nit and Co-Hyd are 56% and 60% respectively, which are significantly higher than those of Co-Ace (12%) and Co-Chl (7%); these results are consistent with the catalytic behavior predicted by TPR results (Fig. 3) that show low-reduction temperatures and high reducibility for Co-Nit and Co-Hyd (Table 1). CO conversions are consistent with TOF for all catalysts (Table 1) and activity decreases in the following order: Co-Hyd > Co-Nit > Co-Ace > Co-Chl. The relatively low activity of Co-Ace is ascribed to the inappropriate electronic states that limit the dissociative adsorption of the CO molecule as explained by Bae et al. [12]. Also, residual Cl⁻ present in Co-Chl has been shown to act as a catalyst poison that lowers the CO conversion [22]. Our XPS analysis (survey scan and atomic composition in Fig. S3 and Table S3) confirm the presence of Cl - impurities in the Co-Chl catalyst.

FTS reaction rate and CO conversion increase in the following order: Co-Chl < Co-Ace < Co-Nit < Co-Hyd. A strong correlation exists between catalytic activity and reducibility obtained from TPR. The higher activity of Co-Nit and Co-Hyd in comparison to Co-Ace and Co-Chl is directly related to the reducibility of the catalysts. Plots of CO conversion as a function of time on stream (TOS) in Fig. 5 show that the catalysts exhibit different stability patterns during FTS. Co-Nit shows good stability as CO conversion only dropped from 65% to 55% and the total CO conversion decreased by only 15%. Co-Hyd also shows high CO conversion (> 50%), but with a profile that suggests gradual catalyst deactivation with time or requires longer time to reach steady state. The CO conversion of Co-Ace dropped from 36% to 12% before reaching a steady state; the total loss of activity in terms of CO conversion is as high as 67%, which may be attributed, in part, to the low catalyst stability. Similarly, Co-Chl shows poor CO conversion and stability as it drops from 17% to 6%. In the case of Co-Chl, the low CO

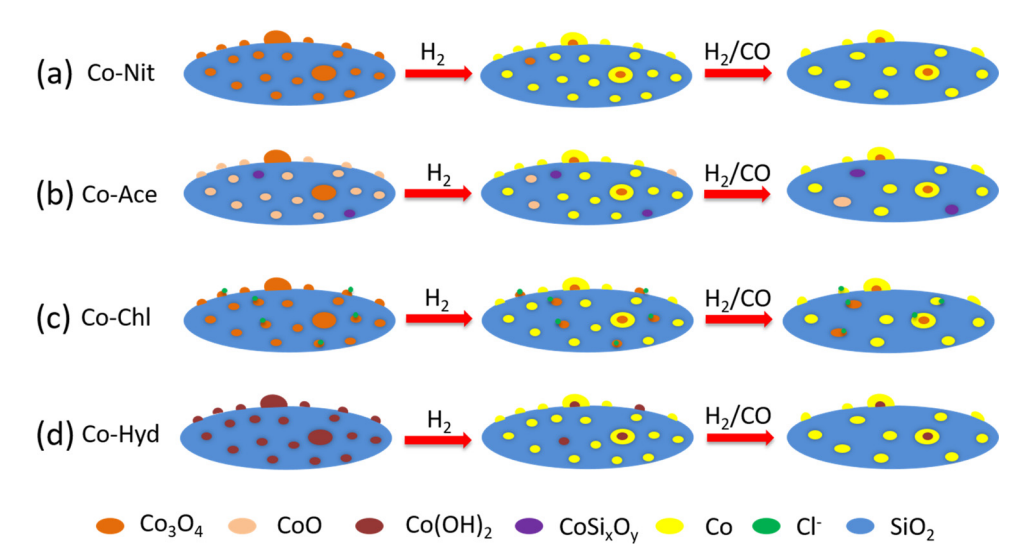


Fig. 11. Schematic illustration of the evolution of cobalt catalysts derived from different precursors during FTS process (activation and reaction).

conversion could be due to the blockage of the active site by the residual ${\rm Cl}^-$ ions [22].

XRD patterns of used Co-Nit, Co-Ace, Co-Chl, and Co-Hyd catalysts are shown in Fig. 6. Because of the use of crystalline silicon carbide (SiC) as a diluent, the highly intense peaks from the SiC mask most of the Co_3O_4 peaks in the samples. Nevertheless, diffraction peaks at 20 of 41.7° and 45.3° reveal the presence of cobalt carbide (Co_2C) in Co-Ace, Co-Chl, and Co-Hyd catalysts [54,55]. Among the mechanisms proposed to explain catalyst deactivation in FTS reaction, formation of Co_2C is frequently invoked [9,56–58]. We, therefore, speculate that the deactivation observed in Co-Ace, Co-Chl, and Co-Hyd catalysts may be associated with the formation of Co_2C . However, the absence of Co_2C in the XRD pattern of Co-Nit after reaction demonstrates its good stability.

The high-magnification TEM images of the different catalysts after FTS reaction for 30 h are shown in Fig. 7. By comparing the catalyst features of fresh (Fig. 2) and used catalysts (Fig. 7), it is apparent a distinct change occurs in the catalyst morphology, evidenced in the broadening of PSD of catalysts and an increase in average particle size. This could be due to sintering induced by oxidation–reduction cycles on the catalyst surface as reported by Jacob et al. [59]. The average particle sizes of Co-Nit, Co-Ace, Co-Chl, and Co-Hyd (before and after FTS) are (3.7 and 5.2 nm), (3.0 and 13.0 nm), (2.8 and 7.7 nm), and (4.0 and 14.2 nm), respectively. While there is evidence of sintering in the catalysts, it decreases in the following order: Co-Ace > Co-Hyd > Co-Chl > Co-Nit. The stable activity during FTS reaction for Co-Nit is attributed to the low sintering observed. The loss of activity for Co-Ace, Co-Chl, and Co-Hyd may be due to a combined effect of sintering and formation of Co₂C.

3.2.2. Selectivity of SiO₂-supported cobalt catalysts

Table 2 shows the hydrocarbon product distributions of catalysts prepared from different precursors. An additional summary showing the selectivity of the fresh catalysts for the same CO conversion is presented in Table S4. After the reaction reached steady state, the C5+ selectivity increases in the following order: Co-Chl < Co-Ace < Co-Nit < Co-Hyd. Variations of hydrocarbon distribution (C5+ selectivity) as a function of TOS for the catalysts are shown in Fig. 8. The catalysts exhibit different stability patterns. In particular, Co-Nit, Co-Hyd, and Co-Chl exhibit relatively lower C5+ selectivity loss of 20%, 23%, and 24% after 30 h on stream, respectively; in contrast, Co-Ace shows a decrease of 32%. Detailed C5+ product distributions for reactions on all catalysts are summarized in Fig. 9. C5+ product distributions for Co-Ace, Co-Chl and Co-Hyd mainly belong to the diesel range (C12-C17). In stark contrast to Co-Nit, product distribution observed for Co-Hyd is centered on C_{15} , indicating that Co-Hyd-catalyzed FTS reaction is selective for long-chain hydrocarbons. Co-Nit shows a relatively flat distribution, which means more hydrocarbon products are in the gasoline range and the average molecular weight is lower than the other three catalysts. These results are consistent with the chain-growth probability (α) value. The α value of Co-Nit is 0.75, which is lower than those of Co-Ace, Co-Chl, and Co-Hyd with α values of 0.91, 0.88, and 0.86, respectively. Usually, the relationship between C5 + selectivity and α follows a positive trend [3]; however, due to the support confinement effect, their correlation with selectivity may vary [39]. In our case, a positive trend exists between α and C5 + selectivity as catalysts with $\alpha > 0.8$ exhibit high selectivity for long-chain hydrocarbons in the diesel range. Although both Co-Nit and Co-Hyd exhibit relatively high and stable C5+ selectivity, Co-Nit is selective for a broad distribution of hydrocarbons that include low- and high-cut hydrocarbons while Co-Hyd is mainly selective for a high cut. The hydrocarbon selectivity of Co-Hyd is consistent with the high-chain growth probability and may be due to its high reducibility and relatively larger particles that are formed. Co-Ace that seem to experience similar growth in particles also exhibit high α and selectivity for highcut hydrocarbons. In addition, hydroxyl groups have been reported to enhance dispersion, reducibility and catalytic activity of Co [41]. We,

therefore, hypothesize that the hydroxyl groups in Co-Hyd provide an environment that supports improved FTS performance.

3.2.3. X-ray absorption near-edge structure and near-edge X-ray absorption fine structure

Fresh and used Co-Nit and Co-Hyd catalysts were studied using XAS to better understand the influence of precursor and catalytic properties on the local Co structure. Co-Nit and Co-Hyd were primarily examined because they exhibit the highest catalytic activity (Fig. 5) and C5+ selectivity accompanied by different catalyst stability (Fig. 8) and C5+ product distribution (Fig. 9). Co K-edge XANES spectrum has three main regions: pre-edge (A), corresponding to the typically forbidden s→ d transition; absorption edge (B); and a post-edge region (C). In the fresh Co-Nit catalyst (Fig. 10a, black line), the pre-edge feature at 7708 eV and corresponding XANES features are strongly indicative of nanoscale Co₃O₄, consistent with our characterization results from XPS, XRD, and TPR. After FTS reaction, a significant shift in E₀ to lower energy can be observed (Fig. 10b, red line) along with an overall change in XANES profile. The shift to lower E₀ is indicative of a lower overall oxidation state, strongly suggesting formation of CoO and perhaps zerovalent Co. This is consistent with our observations that the conventional Co(NO₃)₂ precursor yields mainly Co₃O₄; the formation of CoO after FTS, as shown in the XANES results, may be due to air oxidation of the reduced sample. The fresh Co-Hyd XANES spectrum (Fig. 10a, blue line) exhibits an E_0 more similar to Co^{2+} materials and profile that would suggest the formation of both α and β Co(OH)₂ [60]. Interestingly, upon undergoing FT reactions for extended periods, the change in local structure is minimal. Near-identical XANES profiles are observed (Fig. 10a, magenta line), which exhibit only a slight broadening of the pre-edge feature and shift to lower E₀. This likely indicates only some of the Co atoms are zerovalent after the reaction. For reference, the XANES of a Co foil (Fig. 10a, green line) is also shown, indicating an overall lack of predominant hcp Co in any of the samples.

The Co K-edge EXAFS are obtained after the data are converted into k-space (with k^2 -weighting) and Fourier transformed from 2.8 to $13.2 \,\text{Å}^{-1}$ (Fig. 10b). Overall, the EXAFS data re-affirm our observations from XANES corresponding to the structural changes observed before and after FTS reaction. Note that all plotted EXAFS distances have not been phase-corrected as presented (~ 0.4 Å). The fresh Co-Nit EXAFS (Fig. 10b, black line) exhibits peaks at 1.47, 2.46, and 2.96 Å, corresponding to the first Co-O coordination sphere and subsequent Co-Co coordination spheres. After FTS reaction, the Co-Nit EXAFS changes drastically (Fig. 10b red), with a highest-magnitude feature aligning with metallic Co at 2.22 Å (Fig. 10b green). In addition, major EXAFS peaks positioned at 1.58 and 2.61 Å correspond to Co-O and Co-Co coordination spheres, respectively, in CoO. The Co-hyd samples, both before and after FTS reaction (Fig. 10b, blue and magenta lines, respectively), exhibit similar features in EXAFS that correspond to a hydroxide structure. The major difference is the appearance of an additional peak in the post-reaction sample at 2.22 Å corresponding to metallic Co.

To quantify these results, EXAFS modeling was performed as described in the experimental section. All fitting results can be found in the Supplementary Information, and local Co coordination numbers (CNs) and nearest neighbor distances (NNDs) are summarized in Tables S5 and S6, respectively. For fresh Co-Nit, three scattering paths were implemented to produce a quality fit using Co-O and Co-Co scattering paths from ${\rm Co_3O_4}$ and an additional Co-O path that more closely resembles a theoretical CoOOH structure [34]. Note this inclusion simply matches features found in the EXAFS but is likely a contribution from either nanoscale distortions within the ${\rm Co_3O_4}$, substrate interactions, and/or backscattering from nitrate left over from the synthesis. The reduced Co-Co CN of 6.61 \pm 0.98 from bulk (12.0) coupled with the modestly high-second Co-O coordination sphere (CN = 4.28 \pm 0.67 and NND of 2.87 \pm 0.01 Å) suggest local nanoscale distortion within these materials. After undergoing FTS, the Co-Nit sample was best

modelled using Co-O and Co-Co scattering paths from CoO, and Co-Co from hcp metallic Co, which reaffirms our XANES observations. CoO local CNs are again significantly reduced from bulk values as expected, while a Co-Co CN of 2.23 \pm 0.29 for hcp Co suggests very small clusters of metallic Co (< 50 atoms) [61]. Co reduction is expected to occur under FTS conditions and our results suggest that re-oxidation after exposure to air is somewhat impeded via stabilization by neighboring hydroxyl groups, thereby preserving the reduced Co clusters. Co synthesized from $Co(OH)_2$ precursor demonstrated markedly different EXAFS modelling results. As synthesized, CNs from the first Co-O and Co-Co coordination spheres are slightly reduced from bulk values $(4.99 \pm 0.74 \text{ and } 4.96 \pm 0.71 \text{ vs } 6.0 \text{ for each, respectively})$, which is common in nanoscale materials. A second Co-O is needed for a sufficient quality fit, with a CN of 4.81 ± 0.97 and an NND of 2.83 ± 0.04 Å. After reaction, a small amount of metallic Co can be modeled, with a Co-Co CN of 1.31 ± 0.25 and a NND of 2.50 ± 0.01 Å. Interestingly, the Co-Hyd is maintained with similar values for Co-O, and Co-Co CNs and NNDs. Unlike Co-Nit, hydroxyl groups from the precursor in Co-Hyd prevents oxidation of metal Co to CoO after FTS reaction. Overall, XANES and EXAFS data confirm the superior structural stability of Co-Hyd and possible presence of hydroxyl groups even after reaction. We conclude that the hydroxyl groups create a basic environment in Co-Hyd that supports stability of Co.

A schematic representation catalyst evolution during H₂ reduction and FTS reaction processes is depicted in Fig. 11. The catalysts are all composed of a small fraction of large particles and a large fraction of small particles. The consistent trend in the average particle size of catalyst obtained from low-magnification TEM and XRD is further evidence of the inability of XRD to detect a large fraction of the small particles (Table S2). Complete reduction of Co-Nit occurs during activation and the catalyst shows mild sintering and high stability, which accounts for its high resistance to deactivation. Co-Ace has a small fraction of Co₃O₄ particles and a large fraction of CoO particles; and as shown by Girardon et al. [20], Co-Ace has a high tendency to form partially reduced Co-Si oxide. Moreover, severe sintering is observed after FTS reaction for Co-Ace. The presence of Cl in Co-Chl results in blockage of active sites and prevents the interaction of H2 with catalysts; therefore, only a small fraction of a Co-Chl catalyst can be reduced. Co-Hyd exhibits high reducibility that is comparable to Co-Nit and the highest TOF, although Co-Hyd appears more prone to sintering during FTS than Co-Nit.

4. Conclusions

A series of SiO2-supported Co catalysts derived from different precursors via incipient wetness impregnation has been studied. The resulting catalyst particles have sizes in a narrow range of 3-4 nm and are well-dispersed on SiO2 support. A catalyst derived from Co(OH)2 (Co-Hyd) shows relatively higher surface area that is ascribed to the unique synthesis method that eliminates the calcination step. The Co phase of the fresh catalyst is sensitive to the Co precursor used during synthesis. A strong correlation between reducibility and catalytic performance is observed; catalysts derived from Co(NO₃)₂ and Co(OH)₂ show higher reducibility (hydrogen consumption > 90%) and catalytic performance (CO conversion and C5 + selectivity) than those from Co(C₂H₃O₂)₂ and CoCl₂. Sintering and Co₂C are observed in Co-Ace, Co-Chl, and Co-Hyd, catalysts that experience different degrees of deactivation. C5+ selectivity increases in the following order: Co-Chl < Co-Ace < Co-Nit < Co-Hyd. C5+ product distributions for Co-Ace, Co-Chl, and Co-Hyd mainly fall in the diesel range (C₁₂-C₁₇), and that for Co-Hyd is centered on C₁₅ and is selective for long-chain hydrocarbons; whereas Co-Nit shows a relatively flat distribution, which means more hydrocarbon products are in the gasoline range. XANES and EXAFS data confirm superior structural stability of Co-Hyd and presence of hydroxyl groups even after reaction. Unlike Co-Nit, the hydroxyl groups create a basic environment in Co-Hyd that may support high TOF and C5+ selectivity.

Acknowledgements

We greatly appreciate financial support from the National Science Foundation under Award Number 1728567. This research used resources of the ISS beamline of the National Synchrotron Light Source II, a U.S. Department of Energy (DOE) Office of Science User Facility operated for the DOE Office of Science by Brookhaven National Laboratory under Contract No. DE-SC0012704. Assistance from Drs. Klaus Attenkofer and Eli Stavitski for XAS measurements is greatly appreciated.

References

- [1] M.E. Dry, The Fischer–Tropsch process: 1950–2000, Catal. Today 71 (2002)
- [2] H. Jahangiri, J. Bennett, P. Mahjoubi, K. Wilson, S. Gu, A review of advanced catalyst development for Fischer–Tropsch synthesis of hydrocarbons from biomass derived syn-gas, Catal. Sci. Technol. 4 (2014) 2210–2229.
- [3] A.Y. Khodakov, W. Chu, P. Fongarland, Advances in the development of novel cobalt Fischer – Tropsch catalysts for synthesis of long-chain hydrocarbons and clean fuels, Chem. Rev. 107 (2007) 1692–1744.
- [4] Q. Zhang, W. Deng, Y. Wang, Recent advances in understanding the key catalyst factors for Fischer–Tropsch synthesis, J. Energy Chem. 22 (2013) 27–38.
- [5] J.M. González-Carballo, F.J. Pérez-Alonso, F.J. García-García, M. Ojeda, J.L.G. Fierro, S. Rojas, In-situ study of the promotional effect of chlorine on the Fischer–Tropsch synthesis with Ru/Al₂O₃, J. Catal. 332 (2015) 177–186.
- [6] E. de Smit, B.M. Weckhuysen, The renaissance of iron-based Fischer–Tropsch synthesis: on the multifaceted catalyst deactivation behaviour, Chem. Soc. Rev. 37 (2008) 2758–2781.
- [7] A.R. de la Osa, A. de Lucas, L. Sánchez-Silva, J. Díaz-Maroto, J.L. Valverde, P. Sánchez, Performing the best composition of supported Co/SiC catalyst for selective FTS diesel production, Fuel 95 (2012) 587–598.
- [8] A.N. Martínez, C. López, F. Márquez, I. Díaz, Fischer–Tropsch synthesis of hydrocarbons over mesoporous Co/SBA-15 catalysts: the influence of metal loading, cobalt precursor, and promoters. J. Catal. 220 (2003) 486–499.
- [9] G.L. Bezemer, J.H. Bitter, H.P. Kuipers, H. Oosterbeek, J.E. Holewijn, X. Xu, F. Kapteijn, A.J. van Dillen, K.P. de Jong, Cobalt particle size effects in the Fischer–Tropsch reaction studied with carbon nanofiber supported catalysts, J. Am. Chem. Soc. 128 (2006) 3956–3964.
- [10] J.-S. Girardon, E. Quinet, A. Griboval-Constant, P. Chernavskii, L. Gengembre, A. Khodakov, Cobalt dispersion, reducibility, and surface sites in promoted silicasupported Fischer–Tropsch catalysts, J. Catal. 248 (2007) 143–157.
- [11] Y. Wang, Z. Tao, B. Wu, J. Xu, C. Huo, K. Li, H. Chen, Y. Yang, Y. Li, Effect of metal precursors on the performance of Pt/ZSM-22 catalysts for n-hexadecane hydroisomerization, J. Catal, 322 (2015) 1–13.
- [12] J.W. Bae, S.-M. Kim, S.-H. Kang, K.V. Chary, Y.-J. Lee, H.-J. Kim, K.-W. Jun, Effect of support and cobalt precursors on the activity of Co/AlPO 4 catalysts in Fischer–Tropsch synthesis, J. Mol. Catal. A Chem. 311 (2009) 7–16.
- [13] H.M. Torres Galvis, A.C.J. Koeken, J.H. Bitter, T. Davidian, M. Ruitenbeek, A.I. Dugulan, K.P. de Jong, Effect of precursor on the catalytic performance of supported iron catalysts for the Fischer–Tropsch synthesis of lower olefins, Catal. Today 215 (2013) 95–102.
- [14] O. Clause, M. Kermarec, L. Bonneviot, F. Villain, M. Che, Nickel(II) ion-support interactions as a function of preparation method of silica-supported nickel materials, J. Am. Chem. Soc. 114 (1992) 4709–4717.
- [15] H. Almkhelfe, X. Li, P. Thapa, K.L. Hohn, P.B. Amama, Carbon nanotube-supported catalysts prepared by a modified photo-Fenton process for Fischer–Tropsch synthesis, J. Catal. 361 (2018) 278–289.
- [16] L.G.A. van de Water, G.L. Bezemer, J.A. Bergwerff, M. Versluijs-Helder, B.M. Weckhuysen, K.P. de Jong, Spatially resolved UV-vis microspectroscopy on the preparation of alumina-supported Co Fischer–Tropsch catalysts: linking activity to Co distribution and speciation, J. Catal. 242 (2006) 287–298.
- [17] E. Iglesia, Design, synthesis, and use of cobalt-based Fischer–Tropsch synthesis catalysts, Appl. Catal. A Gen. 161 (1997) 59–78.
- [18] E. Iglesia, S.L. Soled, R.A. Fiato, Fischer–Tropsch synthesis on cobalt and ruthenium. Metal dispersion and support effects on reaction rate and selectivity, J. Catal. 137 (1992) 212–224.
- [19] E. Iglesia, S.C. Reyes, R.J. Madon, S.L. Soled, Selectivity control and catalyst design in the Fischer–Tropsch synthesis: sites, pellets, and reactors, in: D.D. Eley, H. Pines, P.B. Weisz (Eds.), Advances in Catalysis, eds., Academic Press, 1993, pp. 221–302.
- [20] J.-S. Girardon, A.S. Lermontov, L. Gengembre, P.A. Chernavskii, A. Griboval-Constant, A.Y. Khodakov, Effect of cobalt precursor and pretreatment conditions on the structure and catalytic performance of cobalt silica-supported Fischer–Tropsch catalysts, J. Catal. 230 (2005) 339–352.
- [21] L. Zhang, L. Dong, W. Yu, L. Liu, Y. Deng, B. Liu, H. Wan, F. Gao, K. Sun, L. Dong, Effect of cobalt precursors on the dispersion, reduction, and CO oxidation of CoOx/ γ-Al₂O₃ catalysts calcined in N2, J. Colloid Interface Sci. 355 (2011) 464–471.
- [22] J. Panpranot, S. Kaewkun, P. Praserthdam, J.G. Goodwin, Effect of cobalt

- precursors on the dispersion of cobalt on MCM-41, Catal. Letters 91 (2003) 95–102.
- [23] X. Li, F. Bai, H. Su, Cobalt-based catalysts derived from cobalt carbonyl clusters for Fischer–Tropsch synthesis, Chinese J. Catal. 35 (2014) 342–350.
- [24] S. Sun, N. Tsubaki, K. Fujimoto, The reaction performances and characterization of Fischer–Tropsch synthesis Co/SiO₂ catalysts prepared from mixed cobalt salts, Appl. Catal. A Gen. 202 (2000) 121–131.
- [25] N. Tsubaki, S. Sun, K. Fujimoto, Different functions of the noble metals added to cobalt catalysts for Fischer–Tropsch synthesis, J. Catal. 199 (2001) 236–246.
- [26] J.S. Girardon, E. Quinet, A. Griboval-Constant, P.A. Chernavskii, L. Gengembre, A.Y. Khodakov, Cobalt dispersion, reducibility, and surface sites in promoted silicasupported Fischer–Tropsch catalysts, J. Catal. 248 (2007) 143–157.
- [27] Z. Huang, Y. Zhao, Y. Song, Y. Li, G. Wu, H. Tang, J. Zhao, Study on the oxidation process of cobalt hydroxide to cobalt oxides at low temperatures, RSC Adv. 6 (2016) 80059–80064.
- [28] J. Yang, H. Liu, W.N. Martens, R.L. Frost, Synthesis and characterization of cobalt hydroxide, cobalt oxyhydroxide, and cobalt oxide nanodiscs, J. Phys. Chem. C 114 (2009) 111–119.
- [29] S. Brunauer, P.H. Emmett, E. Teller, Adsorption of gases in multimolecular layers, J. Am. Chem. Soc. 60 (1938) 309–319.
- [30] E.P. Barrett, L.G. Joyner, P.P. Halenda, The determination of pore volume and area distributions in porous substances. I. computations from nitrogen isotherms, J. Am. Chem. Soc. 73 (1951) 373–380.
- [31] H.P. Klug, L.E. Alexander, X-ray diffraction procedures, (1954).
- [32] M.C. Biesinger, B.P. Payne, A.P. Grosvenor, L.W.M. Lau, A.R. Gerson, R.S.C. Smart, Resolving surface chemical states in XPS analysis of first row transition metals, oxides and hydroxides: Cr, Mn, Fe, Co and Ni, Appl. Surf. Sci. 257 (2011) 2717–2730
- [33] B. Ravel, M. Newville, ATHENA, ARTEMIS, HEPHAESTUS: data analysis for X-Ray absorption spectroscopy using IFEFFIT, J. Synchrotron Radiat. 12 (2005) 537–541.
- [34] A. Jain, S.P. Ong, G. Hautier, W. Chen, W.D. Richards, S. Dacek, S. Cholia, D. Gunter, D. Skinner, G. Ceder, K.A. Persson, Commentary: the materials project: a materials genome approach to accelerating materials innovation, APL Mater. 1 (2013) 011002.
- [35] R.J. Berger, J. Pérez-Ramírez, F. Kapteijn, J.A. Moulijn, Catalyst performance testing: radial and axial dispersion related to dilution in fixed-bed laboratory reactors, Appl. Catal. A Gen. 227 (2002) 321–333.
- [36] R. Friedel, R. Anderson, Composition of synthetic liquid fuels. I. Product distribution and analysis of C5–C8 paraffin isomers from cobalt catalyst1, J. Am. Chem. Soc. 72 (1950) 1212–1215.
- [37] G. Jacobs, T.K. Das, Y. Zhang, J. Li, G. Racoillet, B.H. Davis, Fischer–Tropsch synthesis: support, loading, and promoter effects on the reducibility of cobalt catalysts, Appl. Catal. A Gen. 233 (2002) 263–281.
- [38] Ø. Borg, S. Eri, E.A. Blekkan, S. Storsæter, H. Wigum, E. Rytter, A. Holmen, Fischer–Tropsch synthesis over γ-alumina-supported cobalt catalysts: effect of support variables, J. Catal. 248 (2007) 89–100.
- [39] A.Y. Khodakov, A. Griboval-Constant, R. Bechara, V.L. Zholobenko, Pore size effects in Fischer Tropsch synthesis over cobalt-supported mesoporous silicas, J. Catal. 206 (2002) 230–241
- [40] Y. Lu, P. Zhou, J. Han, F. Yu, Fischer–Tropsch synthesis of liquid hydrocarbons over mesoporous SBA-15 supported cobalt catalysts, RSC Adv. 5 (2015) 59792–59803.
- [41] A.Y. Khodakov, W. Chu, P. Fongarland, Advances in the development of novel cobalt Fischer – Tropsch catalysts for synthesis of long-chain hydrocarbons and clean fuels, Chem. Rev. 107 (2007) 1692–1744.
- [42] Ø. Borg, P.D. Dietzel, A.I. Spjelkavik, E.Z. Tveten, J.C. Walmsley, S. Diplas, S. Eri, A. Holmen, E. Rytter, Fischer–Tropsch synthesis: cobalt particle size and support effects on intrinsic activity and product distribution, J. Catal. 259 (2008) 161–164.
- [43] G. Prieto, A. Martínez, P. Concepción, R. Moreno-Tost, Cobalt particle size effects in Fischer–Tropsch synthesis: structural and in situ spectroscopic characterisation on reverse micelle-synthesised Co/ITQ-2 model catalysts, J. Catal. 266 (2009) 129–144.

- [44] E. Lira, C.M. López, F. Oropeza, M. Bartolini, J. Alvarez, M. Goldwasser, F.L. Linares, J.-F. Lamonier, M.J.P. Zurita, HMS mesoporous silica as cobalt support for the Fischer–Tropsch synthesis: pretreatment, cobalt loading and particle size effects, J. Mol. Catal. A Chem. 281 (2008) 146–153.
- [45] P. Concepción, C. López, A. Martínez, V.F. Puntes, Characterization and catalytic properties of cobalt supported on delaminated ITQ-6 and ITQ-2 zeolites for the Fischer–Tropsch synthesis reaction, J. Catal. 228 (2004) 321–332.
- [46] P.A. Chernavskii, A.Y. Khodakov, G.V. Pankina, J.S. Girardon, E. Quinet, In situ characterization of the genesis of cobalt metal particles in silica-supported Fischer-Tropsch catalysts using Foner magnetic method, Appl. Catal. A Gen. 306 (2006) 108–119.
- [47] J.S. Girardon, A. Constant-Griboval, L. Gengembre, P.A. Chernavskii, A.Y. Khodakov, Optimization of the pretreatment procedure in the design of cobalt silica supported Fischer–Tropsch catalysts, Catal. Today 106 (2005) 161–165.
- [48] A.Y. Khodakov, J. Lynch, D. Bazin, B. Rebours, N. Zanier, B. Moisson, P. Chaumette, Reducibility of cobalt species in silica-supported Fischer–Tropsch catalysts, J. Catal. 168 (1997) 16–25.
- [49] S. Karimi, A. Tavasoli, Y. Mortazavi, A. Karimi, Cobalt supported on Graphene a promising novel Fischer–Tropsch synthesis catalyst, Appl. Catal. A Gen. 499 (2015) 188–196.
- [50] B.-A.F. Kengne, A.M. Alayat, G. Luo, A.G. McDonald, J. Brown, H. Smotherman, D.N. McIlroy, Preparation, surface characterization and performance of a Fischer–Tropsch catalyst of cobalt supported on silica nanosprings, Appl. Surf. Sci. 359 (2015) 508–514.
- [51] S.C. Petitto, E.M. Marsh, G.A. Carson, M.A. Langell, Cobalt oxide surface chemistry: the interaction of CoO(100), Co₃O₄(110) and Co₃O₄(111) with oxygen and water, J. Mol. Catal. A Chem. 281 (2008) 49–58.
- [52] Y. Yang, L. Jia, B. Hou, D. Li, J. Wang, Y. Sun, The correlation of interfacial interaction and catalytic performance of N-Doped mesoporous carbon supported cobalt nanoparticles for Fischer-Tropsch synthesis, J. Phys. Chem. C 118 (2014) 268–277.
- [53] M. Davari, S. Karimi, A. Tavasoli, A. Karimi, Enhancement of activity, selectivity and stability of CNTs-supported cobalt catalyst in Fischer–Tropsch via CNTs functionalization, Appl. Catal. A Gen. 485 (2014) 133–142.
- [54] D. Moodley, J. Van de Loosdrecht, A. Saib, M. Overett, A. Datye, J. Niemantsverdriet, Carbon deposition as a deactivation mechanism of cobalt-based Fischer–Tropsch synthesis catalysts under realistic conditions, Appl. Catal. A Gen. 354 (2009) 102–110.
- [55] A. Tavasoli, R.M.M. Abbaslou, A.K. Dalai, Deactivation behavior of ruthenium promoted Co/γ-Al₂O₃ catalysts in Fischer–Tropsch synthesis, Appl. Catal. A Gen. 346 (2008) 58–64.
- [56] J. Xiong, Y. Ding, T. Wang, L. Yan, W. Chen, H. Zhu, Y. Lu, The formation of Co₂ C species in activated carbon supported cobalt-based catalysts and its impact on Fischer–Tropsch reaction, Catal. Letters 102 (2005) 265–269.
- [57] O. Ducreux, J. Lynch, B. Rebours, M. Roy, P. Chaumette, In situ characterisation of cobalt based Fischer–Tropsch catalysts: a new approach to the active phase, Stud. Surf. Sci. Catal. (1998) 125–130.
- [58] V. Gruver, Z. Xiaodong, J. Engman, H.J. Robota, S.L. Suib, M. Polverejan, Deactivation of a Fischer–Tropsch catalyst through the formation of cobalt carbide under laboratory slurry reactor conditions, Preprints-American Chemical Society, Div. Pet. Chem. 49 (2004) 192–194.
- [59] G. Jacobs, P.M. Patterson, T.K. Das, M. Luo, B.H. Davis, Fischer–Tropsch synthesis: effect of water on Co/Al₂O₃ catalysts and XAFS characterization of reoxidation phenomena, Appl. Catal. A Gen. 270 (2004) 65–76.
- [60] R. Ma, Z. Liu, K. Takada, K. Fukuda, Y. Ebina, Y. Bando, T. Sasaki, Tetrahedral Co (II) coordination in α-Type cobalt hydroxide: rietveld refinement and X-ray absorption spectroscopy, Inorg. Chem. 45 (2006) 3964–3969.
- [61] A.I. Frenkel, A. Yevick, C. Cooper, R. Vasic, Modeling the structure and composition of nanoparticles by extended X-Ray absorption fine-structure spectroscopy, Annu. Rev. Anal. Chem. 4 (2011) 23–39.